Modelling an optimised thin film solar cell

Joseph P. Becque[1] and D.P. Halliday[1]

[1] Department of Physics, Durham University, Durham, DH1 3LE, United Kingdom

E-mail: d.p.halliday@durham.ac.uk

Received xxxxxx
Accepted for publication xxxxxx
Published xxxxxx

Abstract

A phenomenological model has been developed to simulate the efficiency of thin film solar cells. The model uses key equations for p-n heterojunctions and includes radiative recombination, Auger recombination, Shockley-Read-Hall recombination and surface recombination losses. This framework is appropriate for final year undergraduate and Masters students. Key solar cell phenomena are related to an equivalent circuit enabling the maximum conversion efficiency to be determined under standard AM1.5 solar illumination. The underlying physical basis of the model is presented together with algorithms to allow numerical simulation of a solar cell under the full range of operating conditions. The simulation accounts for optical losses within the device and uses a shunt resistance to account for recombination losses. Solar cells can be optimised for efficiency, or other operating characteristics, by adjusting layer thicknesses and doping levels. The model is used to investigate an emerging solar technology: thin-film p-n heterojunction Cu_2ZnSnS_4/CdS solar cells. An optimised solar cell is found to have an overall PV conversion efficiency of (10±1)%, however significant uncertainties on the values of some Cu_2ZnSnS_4 material properties mean that the trends predicted by the model are a more useful output from the simulation as these can be related to underlying physical phenomena in a solar cell. A region of maximum efficiency is found for absorber layer thicknesses of the order of microns. The range of CdS thicknesses for which this region is maximised is found when the n-type doping concentration of the CdS is maximised. An abrupt drop in efficiency is found when the CdS doping concentration is less than the doping in the Cu_2ZnSnS_4. Varying device and material parameters provides physical insights into the operation of solar cell devices. Strategies for managing optical losses and carrier losses can be tested leading to the identification of designs optimised for high efficiency thin film solar cells. The model can be used for other thin film PV technologies by inputting material properties.

Keywords: simulation, modelling, solar cells, thin film solar cells, Cu_2ZnSnS_4/CdS solar cells

1. Solar Cells – Introduction

Solar energy presents a promising solution to the world's increasing energy demands and depleting fossil fuel resources, however substantial further cost reduction must be achieved in order for PV solar to be able to compete economically in global energy markets and reach desired Terra-Watt production rates [1]. Thin film solar cells use absorber layers with large absorption coefficients in the order of 10^4 cm^{-1} meaning devices can be made with an absorber layer thickness of the order of micrometres [2, 3], saving on material costs. CdTe and $CuIn_{(1-x)}Ga_{(x)}Se_2$ (CIGS) currently lead in the thin-film market with record efficiencies of 21.5% [4] and 21.7% [5] respectively. This is far below the Shockley-Queisser limit of approximately 30% for

semiconductors with similar band gaps and leaves them behind the efficiencies of other established photovoltaic materials such as c-Si and GaAs, indicating that thin film devices currently available are not fully optimised.

Modelling a thin film solar cell can provide insights on the impact of a range of structural properties of devices and provide a better understanding of how to increase efficiencies and, importantly, which device parameters have the greatest impact on device efficiency. This paper presents a phenomenological model of a thin film solar cell together with a computer algorithm to simulate the device. The model was developed during a Masters project and illustrates how altering device parameters affects device efficiency. The model is tested using a case study simulating a thin film solar cell with an absorber layer made of Cu_2ZnSnS_4 (CZTS) an emerging quaternary chalcogenide semiconductor. The non-toxicity, abundance, and low cost of its constituent elements along with a near optimum 1.5 eV band gap [2, 6, 7] make it a good candidate for future devices. Despite desirable qualities CZTS still suffers from a relatively low efficiency of $(10.0 \pm 0.2)\%$ [8], so simulation can help to find optimised structural parameters that can guide future experimental work.

1.1 Thin Film Solar Cell Structure

Fig. 1 shows a possible substrate arrangement for a thin film solar cell. A substrate layer made of soda lime glass, a web of plastic, or a metal foil, is required to provide mechanical strength. The antireflection coating increases transmission of light into the solar cell [9, 13]; possible materials include TiO_2, Si_3N_4, MgF_2 and SiO_2 [3]. The metal grid can be made of MgF_2 or Ni-Al and is the negative terminal from which electrons carry charge to the external circuit. It is often applied by evaporating on to the transparent conducting oxide (TCO) layer below. The TCO is an essential layer in a thin film solar cell and protects the delicate layers beneath as well as preventing the CdS buffer layer from converting to CdO [14]. TCOs are commonly made of ZnO or ITO and are doped in order to improve electrical conductivity. The metal back layer is often made of Mo, and is the positive terminal of the solar cell connecting to the external circuit.

For the case of solar cells using a CZTS absorber layer, the high density of acceptor point defects and defect complexes [15] means CZTS is only able to function as a p-doped layer and therefore cannot be used as a homojunction. Instead a heterojunction is formed using a second semiconductor, often CdS, as an n-doped buffer layer. The buffer layer is considerably thinner than the p-doped absorber layer and has a larger band gap; this minimises absorption within the buffer layer and maximises transmission into the absorber layer. Often the buffer layer is applied by chemical bath deposition [16, 17]. The CZTS p-doped absorber layer is typically made with a thickness in the order of micrometers because its absorption coefficient is in the order of 10^{-4} cm^{-1} at photon energies above the bandgap. The following sections develop the key relations used in the solar cell model.

1.2 p-n Heterojunctions

Fig. 2**(**a**)** shows a p-n heterojunction energy band diagram in the dark. The junction depicted is a type II staggered interface forming a cliff-like junction in which the conduction band energy of the p-type layer, E_C^p, is greater than the conduction band energy of the n-type layer, E_C^n. It has been shown that this is the junction that forms at a CZTS/CdS interface [18]. An alternative type I heterointerface is formed when $E_C^p < E_C^n$ and produces a spike-like interface which acts as a barrier against current through the junction. Despite this, type II interfaces are considered less favourable because they result in an increased rate of recombination at the interface [19]. This section summarises the key relationships describing a p-n junction which can be found in more detail in any standard semiconductor text.

In the depletion region, there is a uniform charge density on the n- and p-sides given by qN_D and $-qN_A$ respectively, where q is the fundamental unit of charge, N_D is the donor concentration in the n-layer, and N_A is the acceptor concentration in the p-layer. The electric potential, $\phi(x)$, across the depletion region is found from the solution to Poisson's equation,

$$\phi(x) = \begin{cases} qN_D(x + x_n)^2/2\epsilon_r^n\epsilon_0 & -x_n < x < 0\,, \\ qN_A(x - x_p)^2/2\epsilon_r^p\epsilon_0 + \phi_{bi} + \Delta E & 0 < x < x_p\,, \end{cases} \tag{1}$$

where x is the position in the junction, ϵ_0 is the permittivity of free space, ϵ_r^n and ϵ_r^p are the relative permittivities of the n-layer and the p-layer, ΔE is the band offset of either the conduction or the valence band being considered, and ϕ_{bi} is the built in potential. The built in potential is the difference in Fermi levels before the layers are brought into equilibrium. This is given by

$$\phi_{bi} = \frac{1}{q}\left[E_C^n - E_V^p + k_B T \ln\left(\frac{N_A N_D}{N_C^n N_V^p}\right)\right], \tag{2}$$

where, k_B is the Boltzmann constant, T is the temperature, E_C^n and N_C^n are the conduction band energy and the conduction band density of states (DOS) in the n-layer, and E_V^p and N_V^p are the valence band energy and valence band DOS in the p-layer [20].

The depletion widths are found by ensuring continuity of the electric field at the junction interface such that

$$N_D x_n/\epsilon_r^n = N_A x_p/\epsilon_r^p \,, \tag{3}$$

and by considering the boundary conditions on $\phi(x)$ at the interface. This yields

$$x_n = \left[\frac{2\phi_{bi}\epsilon_0\epsilon_r^{n^2}}{q(N_A\epsilon_r^n+N_D\epsilon_r^p)}\frac{N_A}{N_D}\right]^{1/2} \text{ and } x_p = \left[\frac{2\phi_{bi}\epsilon_0\epsilon_r^{p^2}}{q(N_A\epsilon_r^n+N_D\epsilon_r^p)}\frac{N_D}{N_A}\right]^{1/2}. \tag{4}$$

Fig. 2(b) shows a heterojunction under illumination. Photons with energy $E_\gamma > E_G$ generate electron hole pairs. The potential gradient in the depletion region acts on carriers generated in the depletion region, generating a photocurrent, J_γ, flowing from the n-side to the p-side. Additionally, it increases the equilibrium densities of electrons and holes by Δn and Δp respectively (where $\Delta n = \Delta p$). This results in the equilibrium Fermi level splitting into

$$E_{F,n} = E_{F,0} + k_B T \ln\left(\frac{n_0+\Delta n}{n_0}\right) \text{ and } E_{F,p} = E_{F,0} - k_B T \ln\left(\frac{p_0+\Delta p}{p_0}\right), \tag{5}$$

where $E_{F,n}$ and $E_{F,p}$ are the electron and hole quasi-Fermi energies respectively, and n_0 and p_0 are the density of electrons and holes in equilibrium. The majority charge carriers do not experience a significant Fermi level splitting. However, minority carriers in Eq. (5) experience a large shift because Δn and Δp are much greater than their respective equilibrium concentrations. This splitting is equal to the open circuit voltage, V_{OC}, of the solar cell such that

$$qV_{OC} = E_{F,n}^p - E_{F,p}^n = k_B T \ln\left(\frac{(n_0^p+\Delta n^p)(p_0^n+\Delta p^n)}{n_0^p p_0^n}\right). \tag{6}$$

Under this applied voltage, the energy bands on the n- and p-side shift relative to each other, so $\phi(x)$, x_n and x_p in Eq. (1) and Eq. (4) are shifted by $\phi_{bi} \to \phi_{bi} - V_{OC}$. This reduction in the potential barrier causes carrier diffusion across the depletion region to be greater than drift, resulting in a dark current, J_D, flowing from p-side to the n-side of the junction. This current is modelled by the ideal diode equation [20],

$$J_D = J_0\left[\exp\left(\frac{qV_{OC}}{k_B T}\right) - 1\right], \tag{7}$$

where

$$J_0 = q\left(\frac{D_h n_i^{n^2}}{L_h N_D} + \frac{D_e n_i^{p^2}}{L_e N_A}\right), \tag{8}$$

is the saturation current of the diode which depends on the diffusivity of holes and electrons, D_h and D_e, the diffusion lengths of holes and electrons, L_h and L_e, and the material's intrinsic carrier density, n_i. A larger saturation current results in a larger dark current as J_D is directly proportional to J_0.

1.3 Photon Transmission and Absorption

Incident light on a solar cell must reach the absorber layer or buffer layer in order to generate charge carriers that contribute to the current. For light incident on a solar cell at normal incidence, the fraction of photons reflected at each interface within the device is given by the reflectivity, $r(\lambda)$, such that

$$r(\lambda) = \left[\frac{n_1(\lambda) - n_2(\lambda)}{n_1(\lambda) + n_2(\lambda)}\right]^2, \tag{9}$$

where $n_1(\lambda)$ and $n_2(\lambda)$ are the refractive indexes for each material at the interface, and λ is the wavelength of the light. Additionally, in the bulk of each layer in the solar cell, the absorption coefficient, $\theta(\lambda)$, is related to a material's extinction coefficient, $k(\lambda)$, by the relation [20]

$$\theta(\lambda) = \frac{4\pi k(\lambda)}{\lambda}. \tag{10}$$

The extinction coefficient is a measure of the strength of the interaction between incident radiation and the absorber layer determining how quickly the intensity profile decays. The fraction of light absorbed, $a(\lambda)$, over a distance d is given by the Beer-Lambert law [21],

$$a(\lambda) = 1 - \exp(-\theta(\lambda)d). \tag{11}$$

The external quantum efficiency (EQE) of a solar cell is the fraction of minority carriers generated for a given number of incident photons on the device. Assuming that each photon above the band gap energy generates one electron-hole pair, the EQE as a function of photon wavelength for a semiconductor layer that is the j^{th} layer from the top of the device is

$$\text{EQE}_j(\lambda) = a_j(\lambda)\sum_{i=0}^{j-1}(1 - r_i(\lambda))(1 - a_i(\lambda)), \tag{12}$$

where i indexes the layer of the solar cell, starting with $i = 0$ for the atmosphere, then $i = 1$ for the top layer. For a solar photon flux, $\Phi_\gamma(\lambda)$, incident on a solar cell, the photocurrent generated in a semiconductor layer that is j layers from the top, $J_{\gamma,j}$, is [22]

$$J_{\gamma,j} = q\int_0^\infty \mathrm{EQE}_j\,(\lambda)\Phi_\gamma(\lambda)d\lambda\,. \tag{13}$$

The total photocurrent, J_γ, is the sum of the photocurrent generated in each semiconductor layer.

1.4 Recombination

Excited electron-hole pairs have a chance of recombining which reduces the density of photogenerated charge carriers in a solar cell, and therefore limits the current produced by the device. In the dark, the solar cell is in a steady state, so the generation and recombination rates per unit volume, G_0 and R_0, are in thermal equilibrium. However, under illumination there is additional generation, ΔG, equal to the photogeneration rate in the p-n junction. The change in the recombination rate under illumination, ΔR, is governed by several mechanisms where the main ones are: radiative, Auger, Shockley-Read-Hall (SRH), and surface recombination. This section presents the theory describing these mechanisms and introduces formulae [3, 21] which form part of the model.

The mean time a photogenerated carrier will spend in an excited state before recombining is the carrier's lifetime, τ, which is defined as

$$\tau \equiv \frac{\Delta n}{\Delta R}\,. \tag{14}$$

This is related to the diffusion length by

$$L = \sqrt{D\tau}\,, \tag{15}$$

the average distance a carrier will travel before it recombines. The diffusivity, D, is related to the carrier mobility, μ, by the Einstein Relation $D = \mu k_B T/q$ [20]. Carriers inside the depletion region are driven by the electric field and will transit it in the order of picoseconds, much faster than the recombination rate [3]. As a result, any carriers that reach the depletion region will not recombine and will contribute to the load current, but carriers generated outside the depletion region have a chance of recombining. The photocurrent flowing under illumination is due to minority carriers crossing the depletion region which means the current reaching the load in a solar cell is limited by the recombination of minority carriers. Importantly, only the equations governing the recombination of minority carriers are required in the model and thus discussed below.

1.4.1 Radiative Recombination. Radiative recombination between an electron in the conduction band and a hole in the valence band emits a photon. The radiative recombination rate, R_{rad}, is dependent on the densities of both holes and electrons in the semiconductor, hence $R_{rad} = C_{rad}\cdot n\cdot p$ where $n = n_0 + \Delta n$, $p = p_0 + \Delta p$, and C_{rad} is a proportionality constant. Because $\Delta n = \Delta p$, this can be rewritten as

$$R_{rad} = C_{rad}\cdot n_0\cdot p_0 + C_{rad}\cdot \Delta n(n_0 + p_0 + \Delta n)\,, \tag{16}$$

where the second term is the change in the radiative recombination rate under illumination, ΔR_{rad}. From Eq. (14), this gives

$$\tau^n_{rad} = (C_{rad}\cdot n_0)^{-1} \text{ and } \tau^p_{rad} = (C_{rad}\cdot p_0)^{-1}\,, \tag{17}$$

where τ_{rad} is the radiative minority carrier lifetime, and it is approximated that $p_0 \gg n_0 + \Delta n$ in p-type semiconductors and $n_0 \gg p_0 + \Delta p$ in n-type semiconductors. This shows that increasing the doping concentration reduces the lifetime of photogenerated minority charge carriers.

1.4.2 Auger Recombination. In Auger recombination an electron-hole pair recombine and transfer their energy to a third electron (or hole) which moves further into the conduction (or valence) band and then dissipates its energy by emitting a series of low energy acoustic phonons. This process is most likely to involve two electrons and one hole in n-type materials and one electron and two holes in p-type materials. Hence the Auger recombination rates in n- and p-type materials, R^n_{Aug} and R^p_{Aug} respectively, are

$$R^n_{Aug} = C^n_{Aug}\cdot n^2\cdot p \text{ and } R^p_{Aug} = C^p_{Aug}\cdot n\cdot p^2\,, \tag{18}$$

where C^n_{Aug} and C^p_{Aug} are proportionality constants which are approximately equal and the same for all semiconductors because they do not depend on the band structure of semiconductors. Making the same approximations and substitutions as in Eq. (17) gives,

$$\tau^n_{Aug} = (C_{Aug}\cdot n_0^2)^{-1} \text{ and } \tau^p_{Aug} = (C_{Aug}\cdot p_0^2)^{-1}\,, \tag{19}$$

where τ_{Aug}^{n} and τ_{Aug}^{p} are the minority carrier Auger lifetimes in n- and p-type semiconductors. This shows that increasing majority carrier density reduces minority carrier lifetime.

1.4.3 Shockley-Read-Hall Recombination. In SRH recombination, defects in the crystalline structure of a semiconductor lead to energy levels in the energy band gap. CZTS has a very high density of defect states compared to other solar cells and it is believed that SRH recombination is one of the primary reasons higher efficiencies have not been achieved to date [1]. Electrons and holes are able to occupy these defect states and will transit through them when exciting or de-exciting across the band gap. The density of occupied states, n_T, is a Boltzmann distribution proportional to the density of trap states, N_T, and the difference between the trapped state energy, E_T, and the Fermi energy such that $n_T = N_T \cdot \exp[-(E_T - E_F)/k_B T]$. The SRH recombination rates for electrons and holes, $R_{SRH,e}$ and $R_{SRH,h}$, are given by

$$R_{SRH,e} = \sigma_e \cdot v_{th} \cdot (N_T - n_T) \cdot n \text{ and } R_{SRH,h} = \sigma_h \cdot v_{th} \cdot n_T \cdot p\,, \tag{20}$$

where σ_e and σ_h are the capture cross-sections of the electrons and holes, and v_{th} is the thermal velocity of electrons. The recombination rates are maximised for electrons when $n_T = 0$, and maximised for holes when $n_T = N_T$. Hence, from Eq. (14), the minimum lifetimes, $\tau_{SRH,e}^{min}$ and $\tau_{SRH,h}^{min}$, are given by

$$\tau_{SRH,e}^{min} = (\sigma_e \cdot v_{th} \cdot N_T)^{-1} \text{ and } \tau_{SRH,h}^{min} = (\sigma_h \cdot v_{th} \cdot N_T)^{-1}\,. \tag{21}$$

The conditions for these minimum lifetimes are satisfied for trapped states with $E_T \approx E_F$. The SRH recombination rate, R_{SRH}, for an individual trapped state is

$$R_{SRH} = \frac{n \cdot p - n_i^2}{\tau_{SRH,h}^{min}\left[n + N_C \cdot exp\left(\frac{E_T - E_C}{k_B T}\right)\right] + \tau_{SRH,e}^{min}\left[p + N_V \cdot exp\left(\frac{E_V - E_T}{k_B T}\right)\right]}, \tag{22}$$

and hence the lifetimes of carriers recombining due to SRH recombination are given by

$$\tau_{SRH} = \Delta n / R_{SRH}\,. \tag{23}$$

1.4.4 Surface Recombination. Similarly to SRH recombination, surface defects enable surface recombination by introducing a high density of electron states in the forbidden region which increases the chance of electron-hole annihilation. Surface defects differ from point defects in a crystal in that they have a broad distribution of energies compared with the distinct energy states created by well-defined defects in the bulk. This is due to the large variation in bond disruption that occurs at a surface or an interface.

The rate of surface recombination per unit cross-sectional area of minority carriers in n- and p-type semiconductors, R_{surf}^{n} and R_{surf}^{p}, is proportional to the surface densities of free electrons and holes at the interface, n_s and p_s, the density of surface defects, N_{sd}, and the thermal velocity. The proportionality factor for surface recombination is the minority carrier surface velocity, v_{surf}, such that $v_{surf} = \sigma_s v_{th} N_{sd}$, where σ_s is the minority carrier surface capture cross section. Due to recombination occurring in the bulk, fewer carriers reach the surface in a thicker material so the rate is inversely proportional to material thickness, d, such that

$$R_{surf}^{n} = \frac{2 \cdot v_{surf} \cdot n_s}{d} \text{ and } R_{surf}^{p} = \frac{2 \cdot v_{surf} \cdot p_s}{d}. \tag{24}$$

Using Eq. (14), the lifetime of photo-generated charge carriers due to surface recombination, τ_{surf}, is

$$\tau_{surf} = \frac{d}{2 \cdot v_{surf}}. \tag{25}$$

1.5 Equivalent Circuits for Solar Cells

In order to model thin film solar cells, the equivalent circuit shown in Fig. 3 is used. The circuit contains a current generator G_γ, a diode D, a parallel resistor R_P, a series resistor R_S, and a load resistor R_L. The carrier generation due to illumination is represented by G_γ which generates a photocurrent, J_γ, and produces a voltage, V_{OC}. The current flowing through the diode is the dark current, J_D, which only permits current to flow from the p- to n-type layer in the junction (the opposite direction of J_γ), in accordance with the ideal diode equation, Eq. (7).

Recombination in the solar cell can be modelled by a shunt resistance, R_P, where recombination is modelled by a shunt current, J_P, flowing through R_P and hence never reaching the external circuit [3]. When the recombination lifetimes are short, R_P is low. This reduces the current flowing through the external circuit, decreasing power output through the load. From the

recombination lifetimes due to various recombination mechanisms discussed in section 1.4, the total lifetime, τ_{tot}, of a photogenerated minority charge carrier can be found using

$$\frac{1}{\tau_{tot}} = \frac{1}{\tau_{rad}} + \frac{1}{\tau_{Aug}} + \frac{1}{\tau_{SRH}} + \frac{1}{\tau_{surf}}. \quad (26)$$

The series resistance, R_S, is the resistance to current flow through the solar cell and is due to each layer's bulk resistivity and the contact resistances between each layer. This must be minimised in order to optimise the solar cell efficiency because the voltage drop across R_S causes an equivalent reduction to the voltage across R_L.

To find the total current flowing through the external circuit, J_L, the sum of the currents through each component of the circuit is considered,

$$J_L = J_\gamma - J_D - J_P = J_\gamma - J_0\left[\exp\left(\frac{qV_{OC}}{k_B T}\right) - 1\right] - \frac{V_{OC}}{R_P}, \quad (27)$$

and V_{OC} can be written in terms of the potential across the load, V_L, according to

$$V_{OC} = V_L + J_L \cdot R_S. \quad (28)$$

This can be solved for the current voltage relation across the load resistor, which can be used to optimise the power output, $P_{out} = V_L \cdot J_L$, by varying R_L to enable the modelled solar cell to operate at the maximum efficiency point on the $J\,V$ curve. The current voltage relation can also be described by its open circuit voltage, V_{OC}, short circuit current, J_{SC}, and fill factor, FF. V_{OC} is the voltage across the load resistor when R_L is infinite and J_{SC} is the current through the load when R_L is zero. The fill factor is given by $P_{out}/(J_{SC} \cdot V_{OC})$ which gives a measure of the solar cell's quality as it is affected by R_S, R_P,τ_{tot} *and* J_0.

2 The Model

The flow diagram in Fig. 4 shows the algorithms of the program used to model a TiO_2/ZnO/CdS/CZTS/Mo solar cell with a structure as shown in Fig. 1. The depth and doping concentrations of the CZTS absorber layer and CdS buffer layer are varied in order to optimise the efficiency and to study their impact on solar cell outputs. Sample code and program files are available [23].

Each box in Fig. 4 denotes a section of code in the model. The section titled 'Calculate photon transmission and absorption' indicates where the transmission and absorption coefficients are calculated using Eq. (9) and Eq. (10). The section 'Calculate carrier generation as a function of depth' shows where Eq. (11) was used to calculate the rate of electron and hole generation as a function of depth through the CZTS and CdS layers. The section 'Calculate total photogenerated current' sums the electron and hole generation as a function of depth from the previous box across all depths in the absorber and buffer layer (as in Eq. (13)) which gives the total rate of generation of charge carriers. This is equivalent to the total photogenerated current, J_γ. The electron and hole generation as a function of depth is also used in the section 'Calculate shunt resistance'. The depletion region widths calculated with Eq. (4) and the minority carrier lifetimes calculated with Eq. (26) are used to find the open circuit shunt current, and the open circuit voltage is calculated with Eq. (6)**.** Knowing the open circuit voltage and shunt current means that the shunt resistance can be calculated with $R_P = V_{OC}/J_{P,OC}$.

In the section of code titled 'Model equivalent circuit', the equivalent circuit described in section 1.5 is considered and Eq. (27) is used to find the current voltage relation across the load resistor R_L. In the section 'Calculate solar cell efficiency', the power output across the load is maximised by varying R_L and the solar cell efficiency is found as the fraction of power out over solar power incident on the solar cell. The CZTS and CdS layer depths and doping concentrations are then varied in order to explore how they impact the solar cell efficiency with the entire process being repeated each time. The following subsections expand on each of the boxes shown in Fig. 4.

2.1 Modelling Solar Cell Layers, Generating the Solar Spectrum, and Initialising the Solar Cell

The sections in Fig. 4 titled 'Generate all layer materials' and 'Generate solar spectrum' refer to the defining of each thin film material used and the solar spectrum used as objects that can be handled by the simulation. This means specifying all their physical properties that will be required in the model. With the solar spectrum and solar cell layers defined, they can be combined with chosen layer thicknesses (and doping concentrations for CZTS and CdS) in order to initialise a specific solar cell.

The solar spectrum in this model is defined as an AM1.5G global solar spectrum with a total power of 1000 W m^{-2} over the energy range 0.3 - 4.4 eV [24], and the parameters used to define CZTS and CdS are shown in Table I. Some parameters

required for the model have not been extensively studied or vary widely in literature. Therefore, where available, experimental results obtained for specific CZTS solar cells have been used.

Parameter	**Absorber (CZTS)**		**Buffer (CdS)**	
Energy gap, E_g (eV)	1.32 ± 0.03	[25]	2.34 ± 0.01	[29]
Conduction band DOS, N_C ($\mathrm{cm^{-3}}$)	$(2.2 \pm 0.05) \times 10^{18}$	[31, 32]	$(1.8 \pm 0.05) \times 10^{19}$	[33, 34]
Valence band DOS, N_V ($\mathrm{cm^{-3}}$)	$(1.8 \pm 0.05) \times 10^{19}$	[31, 32]	$(2.4 \pm 0.05) \times 10^{18}$	[33, 34]
MC mobility, μ ($\mathrm{cm^2 \cdot s^{-1} \cdot V^{-1}}$)	6.2 ± 0.05	[9]	25 ± 0.5	[31, 32]
MC capture cross-section, $\sigma_{e,h}$ ($\mathrm{cm^2}$)	$(1 \pm 0.5) \times 10^{-15}$	[3]	$(1 \pm 0.5) \times 10^{-15}$	[3]
MC thermal velocity, v_{th} ($\mathrm{cm \cdot s^{-1}}$)	$(1 \pm 0.5) \times 10^{7}$	[31]	$(1 \pm 0.5) \times 10^{7}$	[31]
Relative permittivity, ϵ_r	7.5 ± 0.3	[25]	5.16 ± 0.005	[35]
MC radiative coeff., C_{rad} ($\mathrm{cm^3 \cdot s^{-1}}$)	$(1.7 \pm 0.2) \times 10^{-10}$	[36]	$(1.7 \pm 0.2) \times 10^{-10}$	[36]
MC Auger coeff., C_{Aug} ($\mathrm{cm^6 \cdot s^{-1}}$)	$(7 \pm 4) \times 10^{-30}$	[36]	$(7 \pm 4) \times 10^{-30}$	[36]
MC surface capture velocity, v_{surf} ($\mathrm{cm \cdot s^{-1}}$)	$(5.5 \pm 4.5) \times 10^{3}$	[37]	1 *	
Density of trapped states, N_T ($\mathrm{cm^{-3}}$)	$(4 \pm 3) \times 10^{18}$ *		$(1 \pm 0.5) \times 10^{17}$	[38]

TABLE I: Simulation parameters for the CZTS absorber layer and the CdS buffer layer. Minority carrier is abbreviated to MC. Values in literature for which no uncertainty was stated have been taken to be accurate to the last significant figure. The values marked with * have been found by calibration.

There is limited information on exact values of the minority carrier recombination coefficients C_{rad}, C_{Aug}, v_{surf}, and N_T because the values determined experimentally are the total lifetimes and the diffusion lengths resulting from the combined impact of all parameters. Instead, values of C_{rad} and C_{Aug} for GaAs have been used for both CdS and CZTS. This is reasonable because C_{rad} should be similar because they are all direct band gap semiconductors, and C_{Aug} is similar for most semiconductors because it does not have strong dependence on band structure [3]. A possible range for the surface recombination velocity in CZTS, v_{surf}^{CZTS}, is proposed to be $10^3 - 10^4$ $\mathrm{cm \cdot s^{-1}}$ [37], and the density of trapped states in CdS, N_T^{CdS}, has been estimated to be $N_T^{CdS} = (1 \pm 0.5) \times 10^{17}$ $\mathrm{cm^{-3}}$ [38]. However, the surface capture velocity in CdS, v_{surf}^{CdS}, and the density of trapped states in CZTS, N_T^{CZTS}, are not determined. These values are calibrated by considering particular instances of depths and doping concentrations for which the minority carrier diffusion lengths of $L_e^{CZTS} = (0.14 \pm 0.03)$ μm [39] and $L_e^{CdS} = (0.25 \pm 0.19)$ μm [40] were measured. To do this, Eq. (15) is used to relate the diffusion lengths with the total carrier lifetimes, τ_{tot}, which is determined from Eq. (26). The radiative, Auger, SRH and surface recombination lifetimes in Eq. (26) are determined from Eq. (17), Eq. (19), Eq. (23), and Eq. (25) respectively, where the required values N_T^{CZTS} and v_{surf}^{CdS} are calculated in Eq. (23) and Eq. (25) respectively. This calibration found $N_T^{CZTS} = (4 \pm 3) \times 10^{18}$ $\mathrm{cm^{-3}}$ and $v_{surf}^{CdS} = 1$ $\mathrm{cm\ s^{-1}}$. The uncertainty on calibration parameters means that the uncertainty of v_{surf}^{CdS} extends from 0.1 - 10^5 $\mathrm{cm\ s^{-1}}$. This range is so great because under the calibration constraints, SRH recombination is the dominant recombination mechanism, so changes in v_{surf}^{CdS} do not significantly affect L_e^{CdS}.

The conduction and valence band offsets used are $\Delta E_C = (0.01 \pm 0.01)$ eV, and $\Delta E_V = (1.30 \pm 0.04)$ eV. These are determined from literature values [19] and adjusted to the band gaps of the CZTS and CdS samples used in this model while maintaining the ratio $(E_G^{CZTS} + E_G^{CdS})/(\Delta E_C + \Delta E_V)$.

2.2 Photon Transmission and Absorption

The management of light by the solar cell is modelled in the code section titled 'Calculate photon transmission and absorption' in Fig. 4. At this point in the model, the reflectivity at each interface as a function of wavelength, $r(\lambda)$, is calculated from the refractive indexes of each layer, $n(\lambda)$, by using Eq. (9). Additionally, the fraction of light absorbed within the bulk of each layer as a function of wavelength, $a(\lambda)$, is calculated using the Beer-Lambert law, Eq. (11), where the absorption coefficients, $\theta(\lambda)$, are found from each material's extinction coefficients, $k(\lambda)$, using Eq. (10). This enables the intensity profile of the light as a function of wavelength and position to be simulated as it passes through each layer of the solar cell. The refractive indexes for the layers are large and similar in magnitude, so the reflection coefficients are small. As a result, the fraction of light making multiple reflections before being transmitted is negligible and therefore only the first reflection of light is considered in calculations of light intensity.

The refractive indexes, $n(\lambda)$, and extinction coefficients, $k(\lambda)$, for the CZTS used in this model were obtained from a 1.32 eV band gap CZTS thin film, created by co-evaporation onto a quartz substrate [25]. The numerical data of $n(\lambda)$ and $k(\lambda)$ used for the TiO_2 [26], ZnO [27,28], CdS [29], and Mo [30] layers is available [23].

2.3 Carrier Generation as a Function of Depth

This subsection refers to the section 'Calculate carrier generation as a function of depth' in Fig. 4. Within the p-n junction, the absorption of photons is calculated as a function of depth and wavelength using the Beer-Lambert law, Eq. (11). Each photon with $E_\gamma > E_g$ is modelled to generate one electron and one hole via a direct transition at the Γ point which in this model both thermalise instantaneously to the conduction and valence band edges respectively. Hence the rate of photon absorption as a function of depth is equivalent to the rate of carrier generation per unit volume as a function of depth in each layer of the p-n junction. In order to model this, the solar cell layers are divided into discrete intervals of depths, and the carrier generation per unit area per depth interval is calculated. This is where the majority of the computation time arises for the model because Eq. (11) must be calculated for every interval of depth for every interval of photon wavelength. The light reflected at the back of either the CdS buffer or CZTS absorber layer and travelling back towards the top of the solar cell also contributes to the generation rate, but any successive reflections are disregarded because of the low reflection coefficients.

2.4 Total Photogenerated Current and Shunt Resistance

In the code section titled 'Calculate total photogenerated current' in Fig. 4, the total rate of photogenerated electrons and holes per cross-sectional area in each layer is found by summing the carrier generation rate as a function of depth over the whole depth of the n-doped layer and p-doped layer, according to Eq. (13). This is equivalent to the total photogenerated current, J_γ.

In this section the shunt resistance, R_P, is found using $R_P = V_{OC}/J_{P,OC}$. V_{OC} is the open circuit voltage calculated using Eq. (6) and $J_{P,OC}$ is the open circuit shunt current which is equivalent to the rate of recombination in the p-n junction. All recombination events are assumed to be independent and occur at a constant rate per unit volume, R, meaning they can be modelled as a Poisson distribution. However, R is very large (much larger than Avogadro's number), so the recombination is very accurately modelled by a normal distribution with a mean and a variance of R. To calculate the rate of recombination within the absorber and buffer layers, the normal distribution of decay rates is transformed into a normal distribution of diffusion lengths of minority carriers with a mean distance L using Eq. (14) and Eq. (15). Because this is a normal distribution, an equal number of carriers can be considered to travel a greater distance than the mean compared to the number travelling a distance less than the mean. As a result, the probability of a generated carrier existing at any distance from where it was generated can be approximated as a step function, where the step occurs a distance L from the point of generation. Given that the location and the rate of carrier photogeneration within the p-n junction is known, the rate of charge carriers failing to reach the depletion region per unit area is also known. The model assumes carriers generated a distance greater than their diffusion length from the edge of the depletion region will not reach the depletion region and will recombine. The rate at which these carriers recombine is $J_{P,OC}$, hence it is necessary to know the minority carrier diffusion lengths in CZTS and CdS, L_e^{CZTS} and L_h^{CdS}, and the depletion widths in CZTS and CdS, x_{CZTS} and x_{CdS}, in order to calculate the shunt current.

The minority carrier diffusion lengths are found by considering the recombination lifetimes on each side of the p-n junction due to radiative, Auger, SRH, and surface recombination. Each corresponding lifetime, τ_{rad}, τ_{Aug}, τ_{SRH}, and τ_{surf}, is calculated using Eq. (17), Eq. (19), Eq. (23), and Eq. (25) respectively. In CZTS, there are several known defects that create energy levels within the forbidden gap. Taking into account each individual defect state's energy level and formation energy [41], the SRH lifetimes are calculated. Using this, the total minority carrier lifetimes, τ_{tot}^{CZTS} and τ_{tot}^{CdS}, are calculated with Eq. (26), the diffusivity is found using the minority carrier mobilities given in Table I and the Einstein relation, and hence the minority carrier diffusion lengths are calculated with Eq. (15).

The depletion widths in CZTS and CdS, x_{CZTS} and x_{CdS}, are calculated using Eq. (4). The quantities necessary for this calculation are declared when the solar cell layers are generated, as described in section 2.1, and the built in potential, ϕ_{bi}, is calculated using Eq. (2). If the layer depths and doping concentrations of CdS and CZTS are such that either of their depletion widths would exceed the widths of their respective layers, then their size is restricted to be equal to their layer width. Moreover, if the depletion width on one side of the junction is restricted, then continuity in the electric field across the junction is conserved by enforcing Eq. (3). Hence the depletion width on the other side junction will also be reduced.

2.5 Modelling an equivalent Circuit and Calculating Solar Cell Efficiency

In the code section 'Model an equivalent circuit' in Fig. 4, all components of Eq. (27) and Eq. (28) must be known in order to simulate an equivalent circuit and to determine the current voltage relation for the load resistor. The photogenerated current, J_γ, and the shunt resistance, R_p, are calculated as explained in section 2.4, and the saturation current, J_0, which is necessary to calculate the dark current, J_D, is calculated using Eq. (8). Additionally, a fixed value for the series resistance, R_S, is used; although changing the layer thicknesses and doping concentrations will have an impact on R_S, this is beyond the scope of this paper due to the increased complexity this would add. For a CdS/CZTS solar cell, R_S has been experimentally determined to have values in the range of 3.4 $\Omega \cdot \text{cm}^2$ to 6.1 $\Omega \cdot \text{cm}^2$ [12, 42, 43, 44]. For the model, an intermediate value of $R_S = 4.1\ \Omega \cdot \text{cm}^2$ is used [43].

A load resistance is chosen for which the current voltage relation gives the maximum power output, P_{out}, and the solar cell's efficiency, η, is calculated using $\eta = P_{out}/P_{in}$ where P_{in} is the incident power on the solar cell from the AM1.5 solar spectrum.

2.6 Varying CZTS and CdS Layer Depths and Doping Concentrations

Solar cells are modelled as the depth of the CZTS layer, d_{CZTS}, is varied from 10 nm to 10 μm, the depth of the CdS layer, d_{CdS}, is varied from 1 nm to 1 μm, and N_A and N_D are both varied between 1×10^{20} m^{-3} and 1×10^{24} m^{-3}. In order to give a complete understanding of what affects CZTS solar cells' efficiencies while maintaining a manageable program run time, two permutations are made. The first varies the doping concentrations at 30 logarithmically spaced intervals within their ranges, while varying the depths at 4 logarithmically spaced intervals within their ranges. The second varies doping concentrations at 4 logarithmically spaced intervals, while varying the depths at 30 logarithmically spaced intervals.

A separate high resolution optimisation routine is used to find solar cell with maximum efficiency, η_{max}, as this set of measurements does not provide great enough resolution. This involves a series of batches of solar cells being generated over a range of doping concentrations and layer depths, N_D, N_A, d_{CZTS}, and d_{CdS}, each of which focuses on the most efficient cell generated in the prior batch. The highest efficiency solar cells generated from each of the original two permutations are used as starting points for the high resolution optimisation routine. This is done by taking the values from the 4-interval arrays for each of N_D, N_A, d_{CZTS}, d_{CdS} that encompass both maxima from the first two batches. Solar cells are then generated at six linearly spaced intervals within each of these ranges, testing a 6×6×6×6 grid of solar cells in total. The cell generated with the highest efficiency from this new batch is chosen as the central point for the next resolution increase. Doping concentrations and depths one interval higher and one interval lower than the maximum efficiency solar cell define the new range over which a higher resolution pass is made. Further higher resolution passes are performed until all intervals are less than 10% of their respective parameters, at which point the uncertainty on any efficiencies calculated due to uncertainty on the input parameters is much greater than any increase in efficiency achieved by further passes.

3 Results and Discussion

For sections 3.1 to 3.5, the outputs from the model are broken down to consider how photon absorption, minority carrier lifetimes, diffusion lengths, depletion widths, shunt current, and efficiency depend on the doping concentrations and layer depths. Trends shown in these outputs can provide an understanding of what mechanisms impact a solar cell's total efficiency and provides insights into how to maximise their efficiency. A physical interpretation of these dependencies is also used to perform a qualitative analysis of the model's accuracy and reliability. As such, trends are considered as opposed to a focus on absolute values and their uncertainty. In section 3.6 a discussion on efficiency optimisation and an error analysis is presented.

3.1 Photon Absorption

Fig. 5 shows the model's prediction of the fraction of photons absorbed in each layer at a given energy. This is equal to the EQE for CdS and CZTS. The graph shows a drop in the EQE of CZTS for energies greater than 2.34 eV, the band gap of CdS. This is as expected and arises from CdS having a larger band gap than CZTS. It therefore removes carriers that would otherwise be absorbed in the CZTS layer. Moreover, the model shows that reducing the thickness of the CdS layer shifts the location of carrier absorption from CdS to CZTS.

3.2 Lifetime and Diffusion Lengths

Fig. 6(a) shows how the lifetimes of minority carriers for each recombination mechanism in CZTS vary with N_A. The solid and dashed lines for SRH and surface recombination lifetimes are for the thickest and thinnest ($d_{CZTS} = 1 \times 10^{-5}$ m and $d_{CZTS} = 1 \times 10^{-8}$ m) CZTS layers tested respectively. The inset shows how surface recombination lifetimes vary with CZTS

depth. There is an uncertainty on the τ_{aug}^{CZTS} and τ_{rad}^{CZTS} because the parameters C_{Aug}^{CZTS} and C_{rad}^{CZTS} used are based on values for GaAs, as discussed in section 2.1. Despite the fact that both CZTS and GaAs are direct band gap semiconductors, GaAs has a monocrystalline structure whereas CZTS is polycrystalline. The impact of this is negligible though because the figure shows that SRH and surface recombination dominate at all doping concentrations and depths tested by the model. This is in agreement with theory because CZTS forms a high concentration of defects in the bulk and at interfaces. This supports the value of v_{surf}^{CZTS} used in the model, and suggests that the calibration of N_T^{CZTS} yields a reasonable value.

The combined impact of all recombination mechanisms on the diffusion length of minority carriers in CZTS for this model is shown in Fig. 6(b). For $d_{CZTS} = 1 \times 10^{-7}$ m and $d_{CZTS} = 1 \times 10^{-8}$ m, the transition between surface recombination dominating to SRH recombination being dominant can be seen at the doping concentration at which L_e^{CZTS} begins to decrease with N_A. This occurs at lower doping concentrations for thicker d_{CZTS} because according to Eq. (25) the impact of surface recombination is less at thicker depths. When $d_{CZTS} = 1 \times 10^{-5}$ m and $d_{CZTS} = 1 \times 10^{-6}$ m, the model finds that CZTS is so thick that the impact of surface recombination is minimal and τ_{SRH}^{CZTS} is shortest at all doping concentrations.

3.3 Diffusion Lengths and Depletion Widths

In the model, carriers generated at a distance greater than their diffusion length from the depletion region edge will recombine and contribute to the shunt current. This means $L_e^{CZTS} + x_{CZTS}$ and $L_h^{CdS} + x_{CdS}$ define the maximum distances from the p-n interface that carriers can be generated in CZTS and CdS respectively and still contribute to current in the external circuit. When $L_e^{CZTS} + x_{CZTS} > d_{CZTS}$, carriers generated anywhere in the CZTS layer reach the depletion region, so there is no CZTS shunt current and the shunt resistance in CZTS is infinite. Fig. 7 shows how $L_e^{CZTS} + x_{CZTS}$ varies as a function of N_A. Each sub-plot shows solar cells generated with different d_{CZTS} and each coloured curve is for solar cells with different N_D. The solid and the dashed lines show how $L_e^{CZTS} + x_{CZTS}$ varies for cells at the maximum and minimum d_{CdS} tested respectively. The horizontal black line is the depth of the CZTS layer for the solar cells being tested. If $L_e^{CZTS} + x_{CZTS} < d_{CZTS}$ (below the black line), then electrons generated at the back of the CZTS layer will not be able to reach the depletion region and they will recombine. The distance $d_{CZTS} - (L_e^{CZTS} + x_{CZTS})$ is the distance from the back of the CZTS layer at which carriers will no longer reach the depletion region; the greater this value, the higher the shunt current will be.

The figures all show a decrease in $L_e^{CZTS} + x_{CZTS}$ as N_A is increased. This is because both L_e^{CZTS} and x_{CZTS} decrease with N_A; the diffusion length is shortened because there are more majority carriers with which minority carriers can recombine, and the depletion width in CZTS is shortened because it varies according to Eq. (4) which predominantly depends on the ratio N_D/N_A. This also explains the increase in $L_e^{CZTS} + x_{CZTS}$ observed as N_D is increased at a given N_A.

Additionally, Fig. 7(b), Fig. 7(c), and Fig 7(d) show a discontinuity in $L_e^{CZTS} + x_{CZTS}$, indicated by an abrupt decrease. This can be explained by the restriction of the depletion region to $x_{CZTS} = d_{CZTS}$ whenever it would be greater than the layer thickness. This occurs for a greater range of N_A when N_D is larger.

The range of N_A for which $L_e^{CZTS} + x_{CZTS}$ is greater than d_{CZTS} is large when N_D is maximised. A thinner CZTS layer also increases the range of N_A over which this condition is satisfied. For example in Fig. 7(d), d_{CZTS} is so thin it is satisfied over the whole range tested, whereas in Fig. 7(a) it is not satisfied at all. Moreover, comparison of the curves at thin d_{CdS} and thick d_{CdS} show that a thinner d_{CdS} causes a reduction in $L_e^{CZTS} + x_{CZTS}$. This is because the depletion width in the CdS layer is being restricted by d_{CdS}, and so causes a reduction in x_{CZTS}.

On the basis of this analysis, the model finds that minimising N_A, maximising N_D, and ensuring that d_{CdS} is not so thin that x_{CZTS} is restricted, will maximise the size of x_{CZTS} and result in less recombination in CZTS. The opposite is true for minimising loss of carriers in CdS; x_{CdS} is largest when N_A/N_D is large and a thinner d_{CdS} ensures more carriers reach the depletion region. However, minimising recombination in CZTS is considerably more important because it has been shown in section 3.1 that the majority of carriers are generated in CZTS.

3.4 Shunt Current

Fig. 8 shows how the shunt current at V_{OC} in the CZTS layer varies with the depth of the CdS layer and the CZTS layer for solar cells with different doping concentrations. Each vertex on the surface plot is from a solar cell that has been modelled. The graphs shows how the threshold at which $d_{CZTS} > L_e^{CZTS} + x_{CZTS}$ varies, and how the shunt current increases beyond this threshold. The breaking in the smoothness of the surfaces is due to a rounding error in the calculation of the shunt current. This is discussed in section 3.6.

The figures reveal two distinct mechanisms by which shunt current is produced in this model. One of these, shown by the area labelled B in Fig. 8, is independent of d_{CdS} and occurs when d_{CZTS} is so thick that carriers generated at the back of the

CZTS layer recombine before they reach the depletion region. Increasing the CZTS layer depth increases the number of carriers recombining, leading to a greater shunt current. Comparison of Fig. 8(a) with Fig. 8(b), where N_D has been increased, shows that the threshold point at which $L_e^{CZTS} + x_p = d_{CZTS}$ occurs at larger d_{CZTS} due to the increase this causes in both the width of the depletion region and the diffusion length. When N_A is increased, the threshold is reduced as can be seen by the increased range of d_{CZTS} over which area B extends in Fig. 8(c).

The other mechanism by which shunt current becomes non-zero is dependent on both d_{CdS} and d_{CZTS}, shown by the area labelled A. Here, x_{CZTS} is limited by the thickness of the CdS layer, so if the CdS layer is made thinner, it shortens the depletion region on both sides of the junction. A shunt current is produced as soon as the CdS layer is so thin that x_{CZTS} is reduced such that electrons generated in CZTS can't reach the depletion region. If the CZTS layer is made thicker, a shunt current is produced at a thinner threshold d_{CZTS} than if x_{CZTS} were not being restricted. When N_D is increased, as can be seen by comparison of Fig. 8(b) with Fig. 8(a), the depletion region in CdS gets thinner. This means a thinner CdS layer can be used without reducing x_{CZTS} and causing recombination. This is shown by a reduction in the size of the area labelled A. Moreover, increasing N_D will lead to a thicker depletion region in CZTS, so a thicker CZTS layer can be used without recombination occurring. This means that carrier generation can be maximised in the CZTS layer (with thin CdS and thick CZTS), and recombination in the CZTS layer can be minimised with a large N_D. When N_A is increased, as in Fig. 8(c), the depletion region on the CdS side gets thicker. This means that even at large d_{CdS}, x_{CZTS} is restricted, creating a shunt current. This is shown by the large area of A.

The analysis of the shunt current highlights the importance of considering the impact of doping concentrations on the depletion width to minimise recombination.

3.5 Efficiency

Fig. 9 shows the efficiency, η, of solar cells modelled as d_{CZTS} and d_{CdS} are varied at different doping concentrations. The efficiency of each cell is taken to be the efficiency when the load resistance is optimised to maximise power output at the load. It shows that d_{CZTS} is more dominant than d_{CdS} for increasing the efficiency. This is reasonable because it has been shown in section 3.1 that photon absorption is largely independent of d_{CdS} and predominantly depends on d_{CZTS}. Increasing photon absorption increases J_{SC} and causes a greater quasi-Fermi splitting at the p-n junction, creating a larger V_{OC}. Hence, increasing J_{SC} and V_{OC} will raise the efficiency of the solar cell. This physical description supports the trends shown in the model output. With no recombination, this model suggests that the highest efficiency would be when both layers' thickness is maximised, but recombination at extreme depths limits the benefits of increasing the thickness of layers.

The areas labelled A in Fig. 8, show the shunt current produced in CZTS when x_{CZTS} is restricted. The impact this has on the efficiency can be seen at thin d_{CdS} and thick d_{CZTS}, labelled A in Fig. 9. The reduction in the number of carriers reaching the external circuit creates a drop in efficiency as d_{CdS} decreases.

The model also shows that at very thick d_{CdS}, recombination of photogenerated holes in CdS occurs. This leads to an abrupt decrease in efficiency, labelled C in Fig. 9. This can be explained physically by the fact that the carriers recombining are those furthest from the p-n junction, which for CdS are at the top of the layer, where light enters. Due to the Beer-Lambert law, this is where the rate of generation is greatest. Therefore, there is a greater rate of increase in shunt current as d_{CdS} is increased than when d_{CZTS} is increased. Recombination in CdS causes a sharp decrease in efficiency. This is because increasing the thickness of CdS shifts a proportion of photogeneration from CZTS to CdS, and carriers that are lost would have otherwise been generated in CZTS.

The recombination in CZTS due to thick d_{CZTS} when x_{CZTS} is unrestricted (labelled B in Fig. 8), limits any increase in efficiency greater than a threshold d_{CZTS}. Beyond this point the model finds that the efficiency is flat, labelled area B in Fig. 9. This is because the carriers that are lost to recombination are the same ones that are generated in the extra depth, so the net effect of increasing d_{CZTS} is neutral.

The range of depths encompassed by these three recombination thresholds creates a plateau of maximised efficiency, where the depth of CZTS is in the order of micrometres. The area at which the efficiency is optimised changes with doping concentrations due to their impact on the depletion width and diffusion length, as described in section 3.3. The impact of increasing N_D, shown by comparison of Fig. 9(a) with Fig. 9(b), extends the area to thinner CdS layers because it increases x_{CZTS}, decreases x_{CdS} and increases L_e^{CZTS}. Additionally, the increase in x_{CZTS} and L_e^{CZTS} extends the area to thinner d_{CZTS}, but this is not as significant as the aforementioned change. Conversely, increasing N_D constrains the area at large d_{CdS} because it reduces x_{CdS}, increasing CdS shunt current. Comparison of Fig. 9(a) with Fig. 9(c) shows that increasing N_A expands the area labelled A, completely eliminating the plateau.

Fig. 10 shows how the efficiency varies with doping concentrations at depths that coincide with an area on the plateau. It shows that the efficiency achieved increases with N_A up to a maximum. This increase is due to V_{OC} increasing. Beyond the

maximum, the efficiency decreases with N_A because of the introduction of a shunt current. This is due to x_{CZTS} being restricted by the layer thickness of CdS, corresponding to area A in Fig. 9. As a result, an optimised value of N_A, yields a non-zero shunt current. It also shows that over the ranges tested, N_D should be maximised; reducing N_D results in an abrupt drop in efficiency when x_{CZTS} begins to be restricted by the depth of CdS, also corresponding to area A.

3.6 Optimising Efficiency

An optimisation routine finds that the model has a maximum efficiency, $\eta_{max} = (10 \pm 1)\%$, over the range of layer depths and concentrations that the model was tested. This efficiency is achieved at $N_A = (2.85 \pm 0.07) \times 10^{15}$ cm^{-3}, $N_D = (9.39 \pm 0.06) \times 10^{17}$ cm^{-3}, $d_{CZTS} = (7.87 \pm 0.02)$ μm, and $d_{CdS} < (0.98 \pm 0.03)$ μm. The uncertainty on these parameters is the resolution that the optimisation routine achieves and the uncertainty on η_{max} is due to the uncertainty on the input parameters in Table I.

Output	Value
η (%)	10 ± 1
V_{OC} (mV)	530 ± 40
J_{SC} (mA·cm^{-2})	32.7 ± 0.4
FF (%)	54 ± 2
R_P ($\Omega \cdot$ cm^2)	80 ± 20

TABLE II: Model Outputs at maximised efficiency.

The J-V curve for the optimised solar cell is shown in Fig. 11, and the efficiency, η, open circuit voltage, V_{OC}, short circuit current, J_{SC}, fill factor, FF, and shunt resistance, R_P,for this cell are shown in Table II. In order to evaluate the accuracy of these results, a comparison can be made between these values and reported experimental outputs of CZTS solar cells; a selection encompassing a range of efficiencies is shown in Table III. The best performing CZTS device to date also has an efficiency of 10% in agreement with the optimised cell simulated by this model. Moreover, V_{OC} and fill factor, FF, are also both within one standard deviation of a reported value. This agreement strongly indicates that the methods used to simulate a PV device are correct and yield physical results. The modelled short circuit current density, however, is 49% larger than the highest experimentally reported J_{SC} in Table III. Despite this disagreement, it is still an achievable value and is less than the Shockley-Queisser (SQ) limit of 35.0 mA·cm^{-2} for the 1.32 eV band gap absorber layer used [45]. The disagreement of J_{SC} with values in Table III can be explained by the low band gap of the CZTS sample used to provide data for this simulation. A lower band gap enables the collection of photons with lower energies and hence leads to the generation of more carriers and a greater short circuit current density. Furthermore, the low band gap also explains why V_{OC} at η_{max} for a simulated cell is lower than that achieved by the highest efficiency cells in Table III; reducing E_G reduces the quasi-Fermi level splitting under illumination resulting in a lower V_{OC}. The FF is also low compared to the highest achieving devices, which is due to the low R_P at η_{max} (reported values of R_P are in the order of 200 - 400 $\Omega \cdot$ cm^2 [42, 43, 44]). The reason for such a low R_P and FF when efficiency is maximised can also be attributed to the small band gap of the CZTS sample used for simulation. This is because the reduction it causes in V_{OC} will change the point of maximum efficiency (shown in Fig. 10) to a different balance of open circuit voltage and shunt current.

N_A (cm^{-3})	N_D (cm^{-3})	d_{CZTS} (μm)	d_{CdS} (nm)	V_{OC} (mV)	J_{SC} (mA·cm^{-2})	FF (%)	η (%)	Source
-	-	-	-	708.3	21.77	65.1	10	[8]
-	-	-	70	747.8	19.5	63.2	9.2	[46]
10^{16}	-	0.6	95	661	19.5	65.8	8.4	[9]
-	-	2.1	70	567	22	58.1	7.3	[43]
-	-	0.650	70	587	17.8	65	6.81	[12]
-	-	2.2	70	610	17.9	62	6.77	[42]
2×10^{16}	-	1.24	-	541	13	59.8	4.1	[47]
-	-	0.65	-	420	16.5	53	3.7	[44]

TABLE III: Experimental results reported for solar cells using a CZTS absorber layer and CdS buffer layer, showing a range of efficiencies achieved. Values left blank have not been reported.

Fig. 12 shows how the efficiency in the proximity of η_{max} varies when each of d_{CdS}, d_{CZTS}, N_D, and N_A are varied independently. It shows that the most sensitive parameter affecting the efficiency close to η_{max} is d_{CZTS}. Fig. 12(a) shows that for $d_{CZTS} < x_{CZTS} + L_e^{CZTS}$, the efficiency increases rapidly as the depth increases because it enables the generation of extra carriers which all reach the external circuit without recombining. Beyond this threshold, any extra carriers generated recombine. In Fig. 12(b), it is shown that the efficiency is independent of d_{CdS}, except when $d_{CdS} > x_{CdS} + L_h^{CdS}$ and carriers are lost to recombination. The discontinuity in efficiencies measured close to $d_{CdS} = x_{CdS} + L_h^{CdS}$ is attributed to the rounding error discussed below and has been accounted for in the optimisation. Fig. 12(c) shows the balance that must be made between maximising V_{OC} with large N_A, and maximising x_{CZTS} and L_e^{CZTS} with small N_A. Whereas η is sensitive to N_A, Fig. 12(d) shows N_D is not as important to the maximisation of η. It is, however, critical that $N_D > N_A$, because decreasing N_D below N_A results in a rapid drop in x_{CZTS}, which creates a shunt current in CZTS.

The dominant error on the solar cell outputs is the uncertainty on the properties of CZTS. The errors in Fig. 12 show that the impact of inaccurate inputs creates an uncertainty on both the magnitudes of values calculated, as well as the precise location of threshold points. This highlights the requirement for accurate material parameters to produce reliable absolute values of outputs. Obtaining parameters with which to run the model is not a straightforward process because CZTS is still an emerging material. This means that critical parameters, such as v_{surf}^{CZTS} and N_T^{CZTS}, are not quoted explicitly in literature. Instead, an approximate value of v_{surf}^{CZTS} has been used, and N_T has been calibrated using this and other known values. As a result, they have the greatest fractional uncertainty of all the inputs, and are also the dominant sources of error in the efficiency. Moreover, many parameters vary greatly in literature from those that have been used. For example, values reported for μ_e^{CZTS} range from 0.1 $cm^2 \cdot V^{-1} \cdot s^{-1}$ to 30 $cm^2 \cdot V^{-1} \cdot s^{-1}$ [2, 48, 49].

There is also a rounding error on the calculation of the efficiency. This is due to the method used to calculate carriers lost as shunt current. When the generation of carriers as a function of depth, $G(x)$, is calculated, the semiconductor depth is divided into discrete intervals. Within each interval the generation rate of photons per unit area per interval length is found. However, the sum of the diffusion length and the depletion width yields a value in between two $G(x)$ measurements. Due to the discrete measurement of $G(x)$, there is an over or underestimate of the shunt current at the distances $L_e^{CZTS} + x_{CZTS}$ and $L_h^{CdS} + x_{CdS}$ either side of the p-n junction. This is seen most clearly in Fig. 12(c) and Fig. 12(d) as $L_e^{CZTS} + x_{CZTS}$ and $L_h^{CdS} + x_{CdS}$ change with the input parameters creating discontinuous steps in the data. In order to reduce this error, the intervals of depths are logarithmically spaced, which increases the frequency of $G(x)$ measurements where dG/dx is greatest and hence where the error is largest. The frequency of intervals was also increased, but the computation of $G(x)$ at each photon wavelength is computationally expensive which limits the resolution that can be achieved without creating an impractical program runtime. A compromise of 200 logarithmically spaced intervals within each semiconductor is sufficient ensure it is not the dominant source of error, and to enable accurate analysis of trends in the data.

Further improvements to the accuracy of the simulation could be made by adding more complexity to the model. For example, the contribution of layer resistivity could be accounted for as depths are varied. Also, carrier mobility has been assumed to be independent of doping concentration, but a higher precision could be achieved by considering how increasing doping concentrations impedes on mobility for example through impurity scattering. Other properties that doping concentration will impact include surface recombination velocities, the density of trapped states, and the contact resistance at the interfaces. CZTS is known to have high concentrations of point defects and defect complexes which impact the energy band structure and reduce V_{OC}. Further work linking the presence of these defects to the bandgap and V_{OC} will provide further insights into maximising device efficiency.

4 Conclusions

A phenomenological model for thin film solar cells has been developed based on key physics occurring in p-n heterojunction devices. The fundamental physical processes modelled by key equations are linked to an equivalent circuit allowing exploration of solar cell device performance under a range of operating conditions. The absorption of a solar spectrum through a device is simulated accounting for the wavelength dependence of transmission, reflection and absorption in the bulk of each layer and at the interfaces. This allows for a depth profile of carrier generation as a function of wavelength in the p-n junction to be obtained. The resulting forward bias and photocurrent generated in the junction is determined and an equivalent circuit is considered to find the power output at the load. A fixed series resistance accounts for the resistivity of each layer and contact resistances between them. Photocurrent lost due to recombination of minority carriers is modelled as a current flowing through a shunt resistance. The method of developing this simulation is presented based on the physical fundamentals of known generation and loss mechanisms in PV devices.

The applicability of the model is demonstrated by applying to a thin film CZTS solar cell with a CdS buffer layer; this is an emerging solar PV thin film technology. The model requires knowledge of fundamental materials parameters to produce reliable results. It can be challenging to determine these accurately for some new semiconductor systems. A particular strength of this model is that it can explore trends observed in the outputs as N_A, N_D, and CdS and CZTS layer depths are varied. These trends can be linked to physical phenomena and provide valuable insights into PV device operations. We find that the modelled behaviour of the minority carrier diffusion lengths, shunt current, and efficiency is in alignment with the physical interpretation. Moreover, analysis of the EQE showed that CdS is not critical as a photon absorber, but instead it is important for the purpose of providing the n-doped side to the p-n junction. Analysis of the efficiency revealed that the output power is maximised at a plateau encompassed by recombination thresholds in CZTS and CdS. Maximised efficiency is found to occur for large CZTS depths in the order of micrometres. Additionally, it is shown that the range of CdS depths for which the device is maximised is greatest for large N_D, and that N_A is optimised by balancing a large V_{OC} and a small shunt current. Further improvements to the model could be made by measuring generation rates in the semiconductor layers with a greater frequency in order to reduce a rounding error in the shunt current. An optimised device is found to have an efficiency of $(10 \pm 1)\%$. This is a reasonable output which further supports the validity of the model used. However, there is a large uncertainty in the input parameters of CZTS which reduces confidence in the absolute values of the outputs obtained and the exact location of maximisation. This means the interpretation of the trends shown by the model, and the area where it shows that efficiency is maximised gives a more significant application of the model. In the proximity of optimised efficiency, it is shown that the depth of CZTS is the most sensitive parameter to the efficiency. It is also found that N_D must be greater than N_A to significantly reduce recombination.

This model has been developed during a Masters project. We have demonstrated the usefulness of this model as a teaching tool to illustrate the response of solar cell output parameters to changes in solar cell device configuration. Furthermore we have shown that the model can provide new physical insights into the behaviour of emerging solar technologies that have not previously been explored. A key learning point is that the outputs of the model are only as reliable as the material parameters input into the model. It can be a challenge to determine these for new semiconductor systems. Notwithstanding these limitations this model provides an excellent tool with which to explore the operation of solar PV devices across a broad range of device characteristics, far more so than would be possible through device fabrication and testing.

Acknowledgements

JPB wishes to thank DPH for many interesting discussions and suggestions, and for his excellent guidance and supervision provided over the course of the Masters project.

References

[1] Polman A, Knight M et al. 2016 *Science* **352**
[2] Ito K and Nakazawa T 1988 *Japanese Journal of Applied Physics* **27** 2094
[3] Dittrich T 2015 *Materials Concepts for Solar Cells* (London: Imperial College Press)
[4] Green M A, Emery K et al. 2015 *Prog in Photovolt: Res and Appl* **23** 1-9
[5] Jackson P, Hariskos D et al. 2014 *physica status solidi (RRL) Rapid Research Letters* **9** 1
[6] Persson, C. 2010 *Journal of Applied Physics* **107** 053710
[7] Katagiri, H., Saitoh, K., et al. 2001 *Solar Energy Materials and Solar Cells* **65** 141–148
[8] Green M A, Hishikawa Y et al. 2017 *Prog in Photovolt: Res and Appl* **26** 3–12
[9] Shin, B, Gunawan O et al. 2013 *Prog in Photovolt: Res and Appl* **21** 72–76
[10] Kim G Y, Jeong A R et al. 2014 *Solar Energy Materials and Solar Cells* **127** 129–135
[11] Sousa M, da Cunha A et al. 2014 *Solar Energy Materials and Solar Cells* **126** 101–106
[12] Wang K, Gunawan O et al. 2010 *Applied Physics Letters* **97** 143508
[13] Tanaka T, Sueishi T et al. 2012 *Journal of Applied Physics* **111** 053522
[14] George P J., Snchez A et al. 1995 *Applied Physics Letters* **66** 3624–3626
[15] Chen S, Wang L-W et al. 2012 *Applied Physics Letters* **101** 223901
[16] Timmo K, Kauk-Kuusik M et al. 2017 *Thin Solid Films* **633** 122-126
[17] Guo Q, Ford G M et al. 2010 *Journal of the American Chemical Society* **132** 17384–17386
[18] Santoni A, Biccari F et al. 2013 *Journal of Physics D Applied Physics* **46** 175101
[19] Bao W and Ichimura M 2012 *Japanese Journal of Applied Physics* **51** 10NC31
[20] Nelson, J. 2003 *The Physics of Solar Cells* 1st edition (London: Imperial College Press)
[21] Wurfel P U 2009 *Physics of Solar Cells* 2nd edition (Weinheim: Wiley-VCH)
[22] Fraas L. and Partain L 2010 *Solar Cells and their applications* 2nd edition (Hoboken, NJ: Wiley)
[23] Becque, J. 2018 https://github.com/Joe-Becque/Modelling-Solar-Cells [Accessed 21 Sep. 2018]

[24] Gueymard C 1995 *SMARTS2, a simple model of the atmospheric radiative transfer of sunshine* (Cocoa, Fl: Florida Solar Energy Center)
[25] Li J, Du H et al. 2012 *Opt. Express* **20** A327–A332
[26] Siefke T, Kroker S et al. 2014 *Advanced Optical Materials* **4** 1780–1786
[27] Venger E F, Melnichuk A V et al. 1995 *physica status solidi (b)* **188** 823–831
[28] Park Y S and Schneider J R 1968 *Journal of Applied Physics* **39** 3049–3052
[29] Cardona M, Weinstein M and Wolff G A 1965 *Phys. Rev.* **140** A633–A637
[30] Querry M R 1987 *Optical constants of minerals and other materials from the millimeter to the ultraviolet* (Kansas City, MO: Chemical Research, Development and Engineering)
[31] Adewoyin A D, Olopade M A and Chendo M 2017 *Optik - International Journal for Light and Electron Optics* **133** 122–131
[32] Zhao W, Zhou W and Miao X 2012 In *7th IEEE International Conference on Nano/Micro Engineered and Molecular Systems (NEMS)* 502–505
[33] Patel M and Ray A 2012 *Physica B: Condensed Matter* **407** 4391–4397
[34] Gloeckler M, Fahrenbruch A L and Sites J R 2003 In *3rd World Conference on Photovoltaic Energy Conversion, 2003. Proceedings of* **1** 491–494
[35] Treharne R E, Seymour-Pierce A et al. 2011 *Journal of Physics: Conference Series* **286** 012038
[36] Strauss U, Rhle W W and Khler K 1993 *Applied Physics Letters* **62** 55–57
[37] Hages C J, Carter N J et al. 2014 *Journal of Applied Physics* **115** 234504
[38] Kanevce A, Repins I and Wei S H 2015 *Solar Energy Materials and Solar Cells* **133** 119–125
[39] Courel M, Valencia-Resendiz E et al. 2016 *Solid-State Electronics* **118** 1–3
[40] Oakes J J, Greenfield I G and Partain L D 1977 *Journal of Applied Physics* **48** 2548–2555
[41] Chen S, Yang J-H et al. 2010 *Phys. Rev. B* **81** 245204
[42] Katagiri H, Jimbo K, et al. 2008 *Applied Physics Express* **1** 041201
[43] Ahmed S, Reuter K B et al. 2011 *Advanced Energy Materials* **2** 253–259
[44] Momose N, Htay M T et al. 2011 *Japanese Journal of Applied Physics* **50** 01BG09
[45] Landsberg P T and Markvart T 2012 *Practical Handbook of Photovoltaics* 2nd edition (Boston MA: Academic Press) 63–75
[46] Sun K, Yan C et al. 2016 *Advanced Energy Materials* **6** 1600046
[47] Schubert B, Marsen B et al. 2011 *Prog in Photovolt: Res and Appl* **19** 93–96
[48] Tanaka T, Nagatomo T et al. 2005 *Journal of Physics and Chemistry of Solids* **66** 1978–1981
[49] Liu F, Li Y et al. 2010 *Solar Energy Materials and Solar Cells* **94** 2431–2434

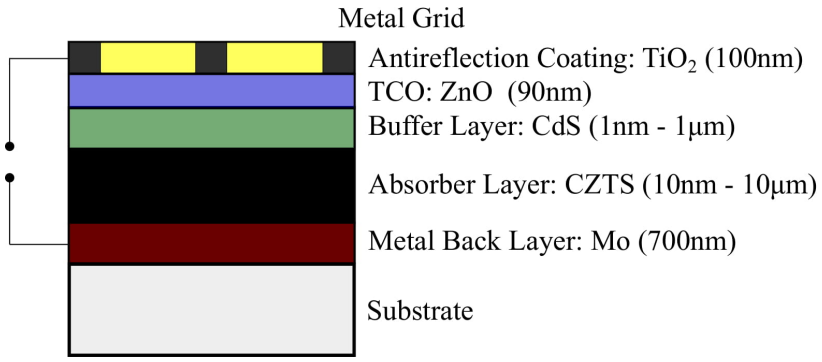

Figure 1: Substrate arrangement of a thin film solar cell. Annotated are the layer types with their typical thicknesses [9-12].

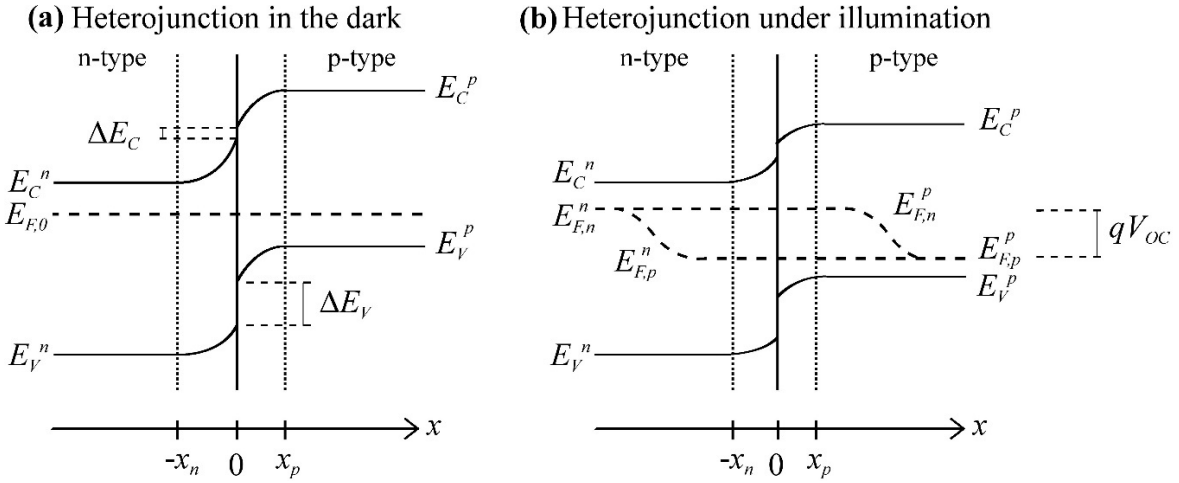

Figure 2: Type II heterojunction (a) in the dark, and (b) under illumination, with conduction and valence band offsets ΔE_C and ΔE_V, and forming depletion a region with widths x_p and x_n either side of the interface. Under illumination, the shared Fermi level, $E_{F,0}$, splits into $E_{F,p}^n$ and $E_{F,n}^n$ on the n-side, and $E_{F,p}^p$ and $E_{F,n}^p$ on the p-side. This creates an open circuit voltage V_{OC}.

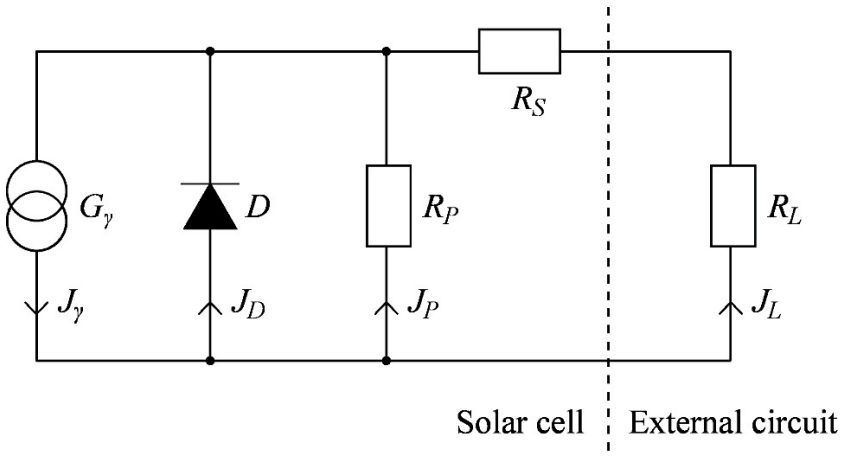

Figure 3: An equivalent circuit for a solar cell containing a photocurrent generator G_γ, a diode D, a parallel resistance R_P, a series resistance R_S, and a load resistance R_L. The vertical dashed line represents the boundary between the solar cell and the external circuit.

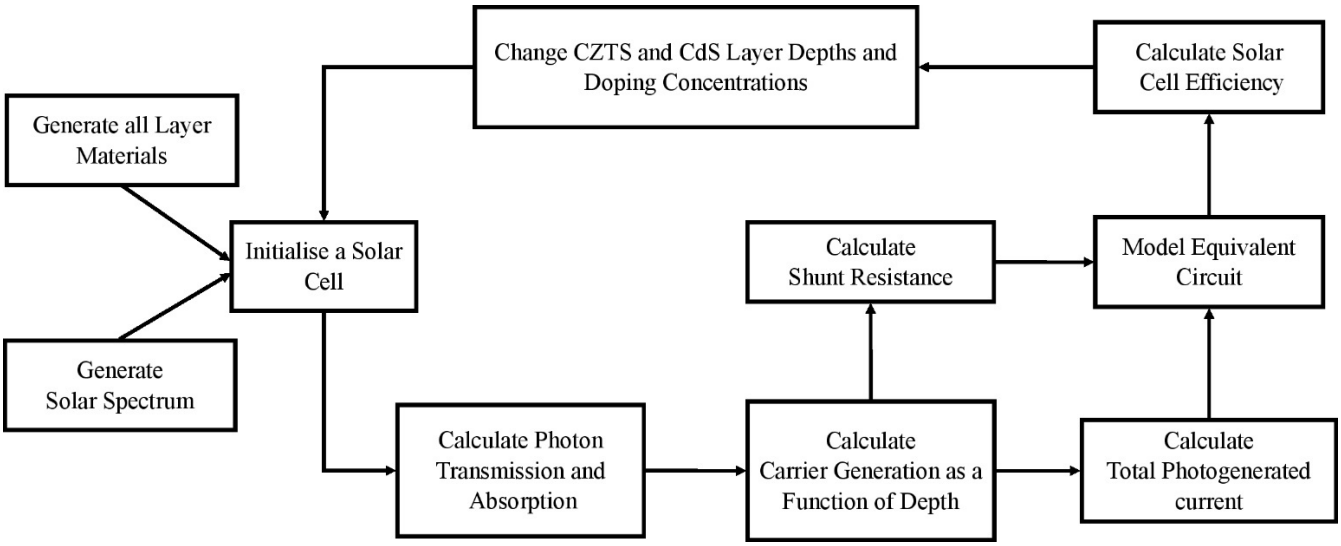

Figure 4: Flow chart illustrating the structure of solar cell model.

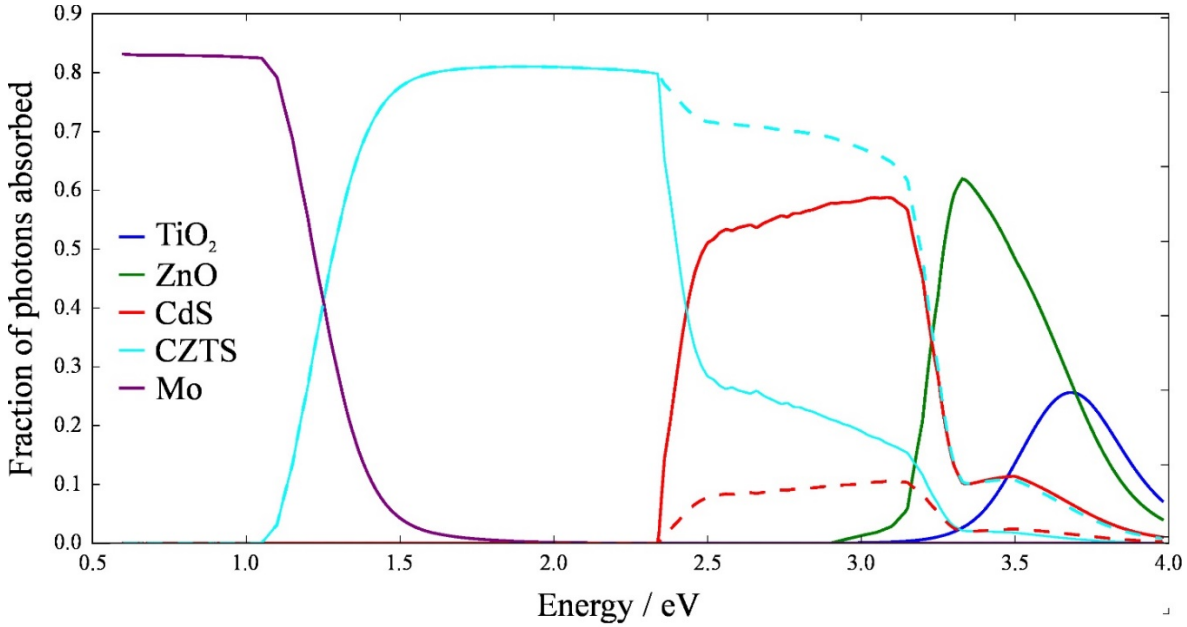

Figure 5: Fraction of photons absorbed in each layer of the solar cell as a function of energy when $d_{CZTS} = 1$ µm. Absorption in the CZTS and CdS at $d_{CdS} = 100$ nm and $d_{CdS} = 10$ nm is shown by solid and dotted lines respectively.

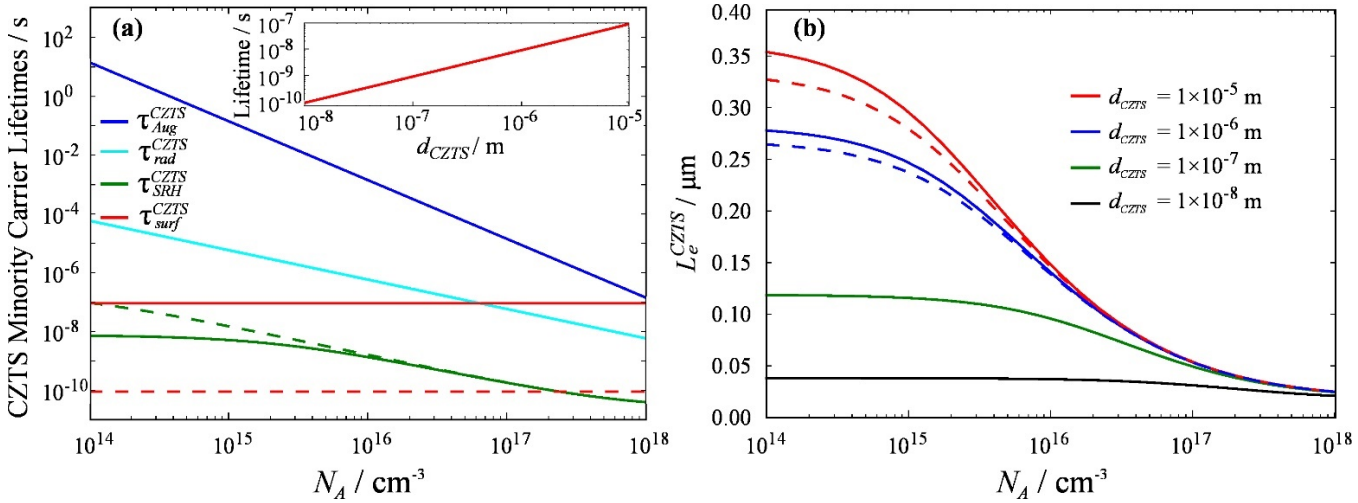

Figure 6: (a) CZTS minority carrier lifetimes of each recombination mechanism as a function of N_A. The dashed lines show $d_{CZTS} = 1 \times 10^{-8}$ m, and the solid lines show $d_{CZTS} = 1 \times 10^{-5}$ m. The inset shows how τ_{surf}^{CZTS} varies with d_{CZTS}. (b) CZTS hole diffusion lengths as a function of N_A at different d_{CZTS}. Solid and dashed lines are at $d_{CdS} = 1$ µm and $d_{CdS} = 1$ nm respectively. This impact of this change is not resolved at $d_{CZTS} = 1 \times 10^{-8}$ m or $d_{CZTS} = 1 \times 10^{-7}$ m.

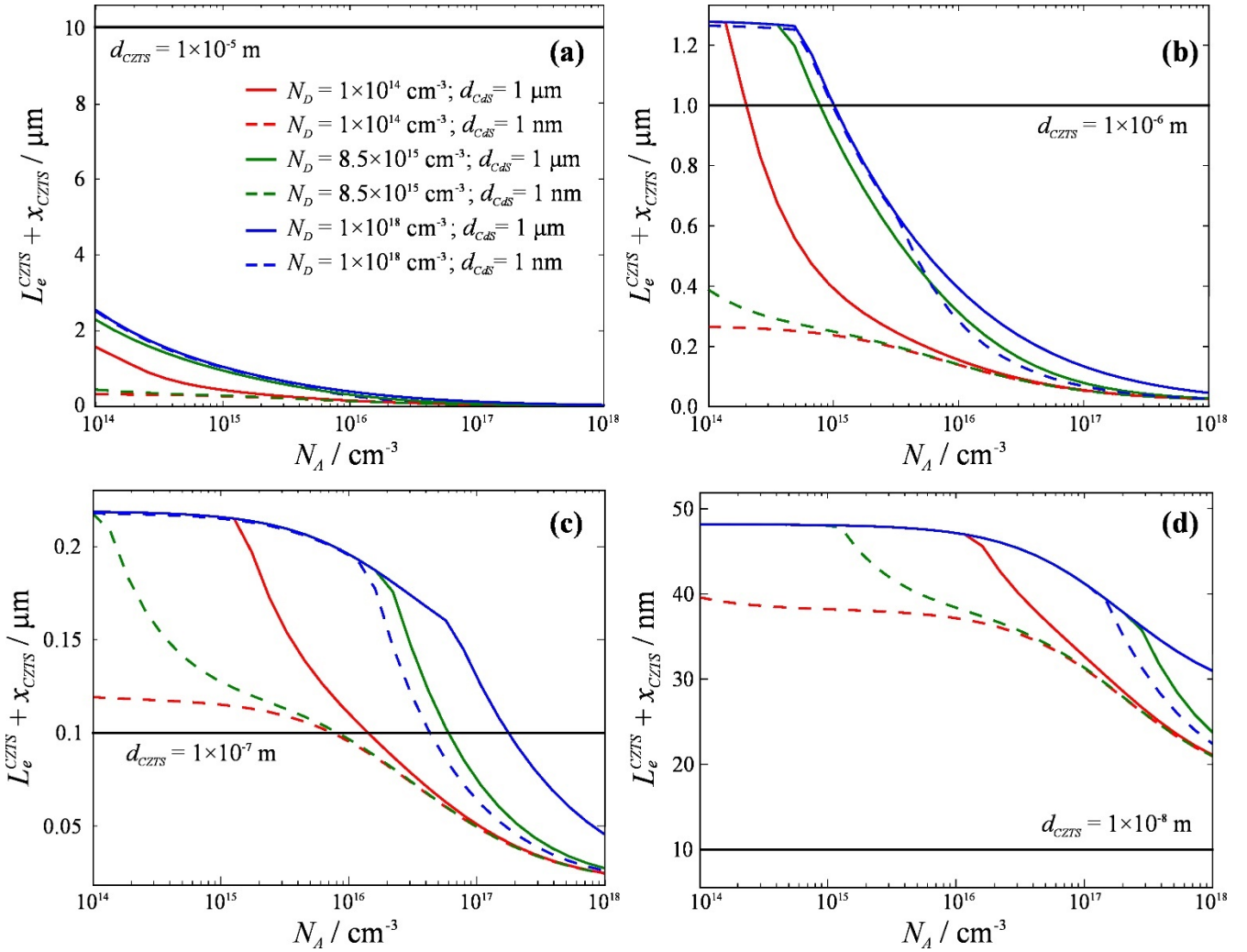

Figure 7: Plots of $L_e^{CZTS} + x_{CZTS}$ as a function of N_A when (a) $d_{CZTS} = 1 \times 10^{-5}$ m, (b) $d_{CZTS} = 1 \times 10^{-6}$ m, (c) $d_{CZTS} = 1 \times 10^{-7}$ m, and (d) $d_{CZTS} = 1 \times 10^{-8}$ m. Different colours indicate different N_D. Solid and dashed lines indicate CdS depths of 1 μm and 1 nm respectively. The black horizontal line indicates the CZTS layer depth. For $L_e^{CZTS} + x_{CZTS} < d_{CZTS}$ there is a non-zero shunt current.

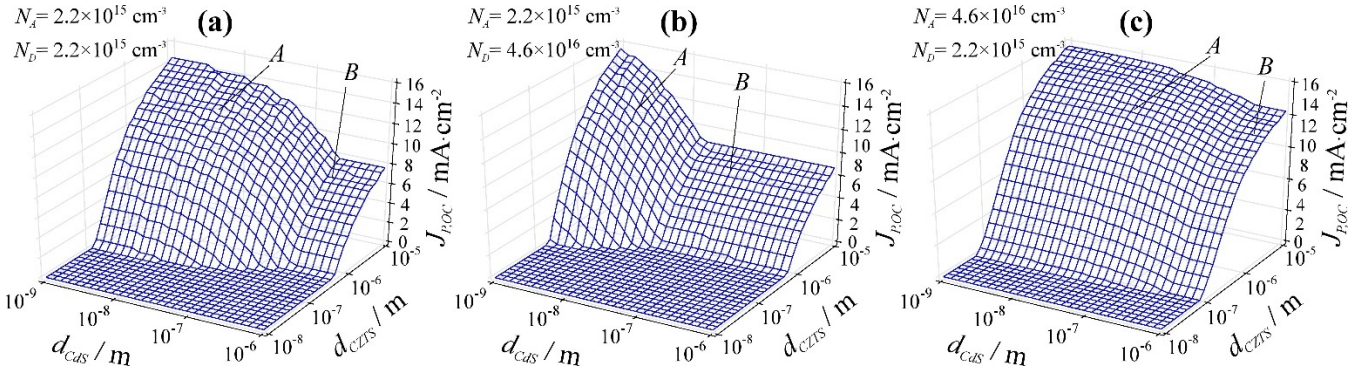

Figure 8: Shunt current at the open circuit voltage, $J_{P,OC}$, in CZTS as a function of CdS and CZTS depths at (a) $N_A = 2.2 \times 10^{15}$ cm^{-3}, $N_D = 2.2 \times 10^{15}$ cm^{-3}, (b) $N_A = 2.2 \times 10^{15}$ cm^{-3}, $N_D = 4.6 \times 10^{16}$ cm^{-3}, and (c) $N_A = 4.6 \times 10^{16}$ cm^{-3}, $N_D = 2.2 \times 10^{15}$ cm^{-3}. The labels *A* and *B* indicate areas impacted by different sources of shunt current. Data has been collected at each vertex and lines connect each point for clarity.

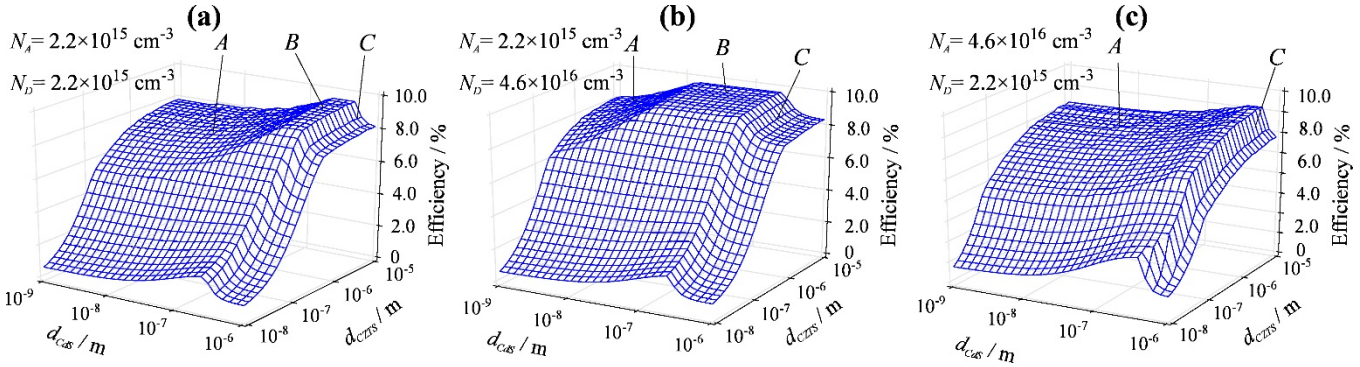

Figure 9: Efficiency as a function of CdS and CZTS depths at (a) $N_A = 2.2 \times 10^{15}$ cm^{-3}, $N_D = 2.2 \times 10^{15}$ cm^{-3}, (b) $N_A = 2.2 \times 10^{15}$ cm^{-3}, $N_D = 4.6 \times 10^{16}$ cm^{-3}, and (c) $N_A = 4.6 \times 10^{16}$ cm^{-3}, $N_D = 2.2 \times 10^{15}$ cm^{-3}. The labels A, B and C indicate the areas impacted by different sources of shunt current. Data has been collected at each vertex and lines connect each point for clarity.

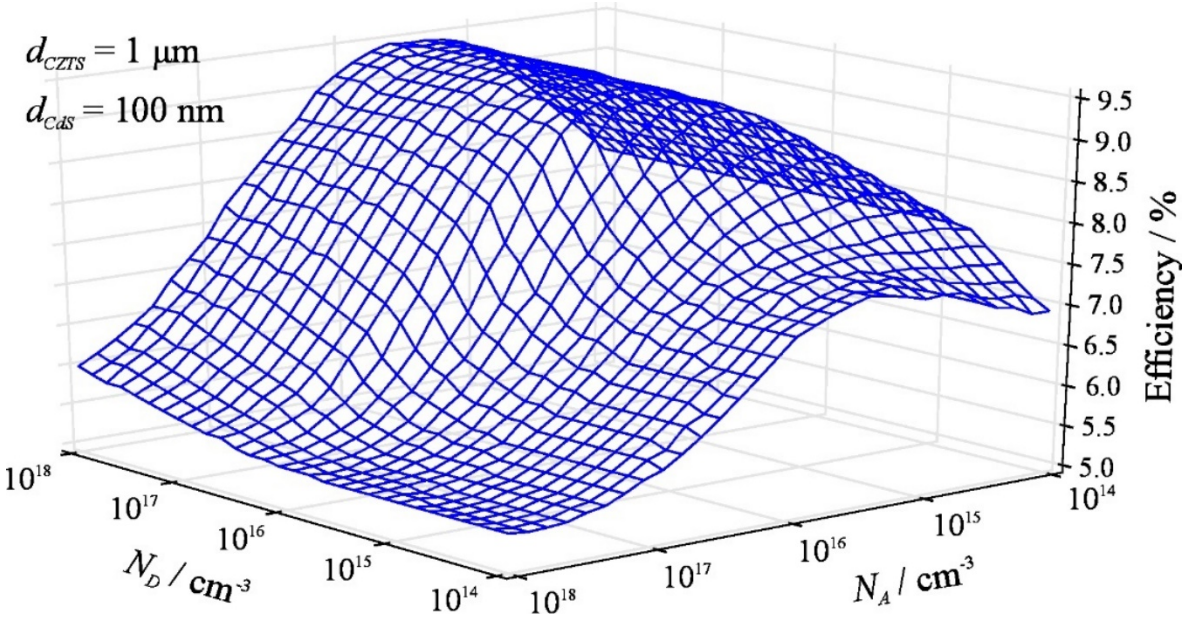

Figure 10: Efficiency of solar cells as N_D and N_A are varied when $d_{CZTS} = 1$ μm and $d_{CdS} = 100$ nm, a point that coincides with the plateau. Data has been collected at each vertex, and lines connect each point for clarity. The axis direction along N_A has also been reversed to give a clearer perspective of the surface.

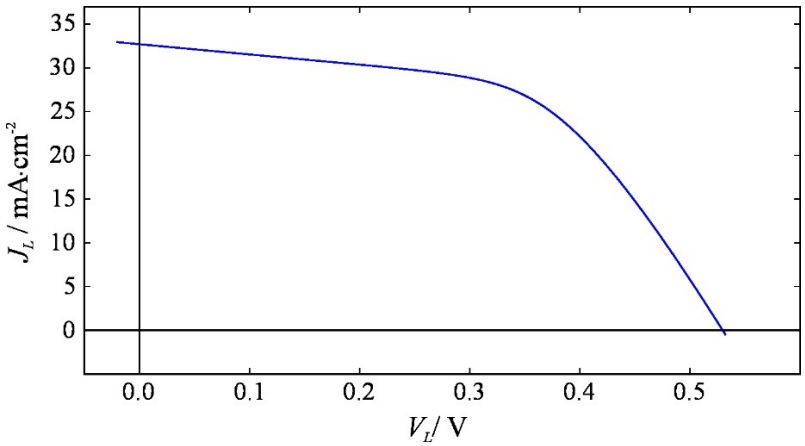

Figure 11: *J-V* curve of an optimized simulated CZTS solar cell.

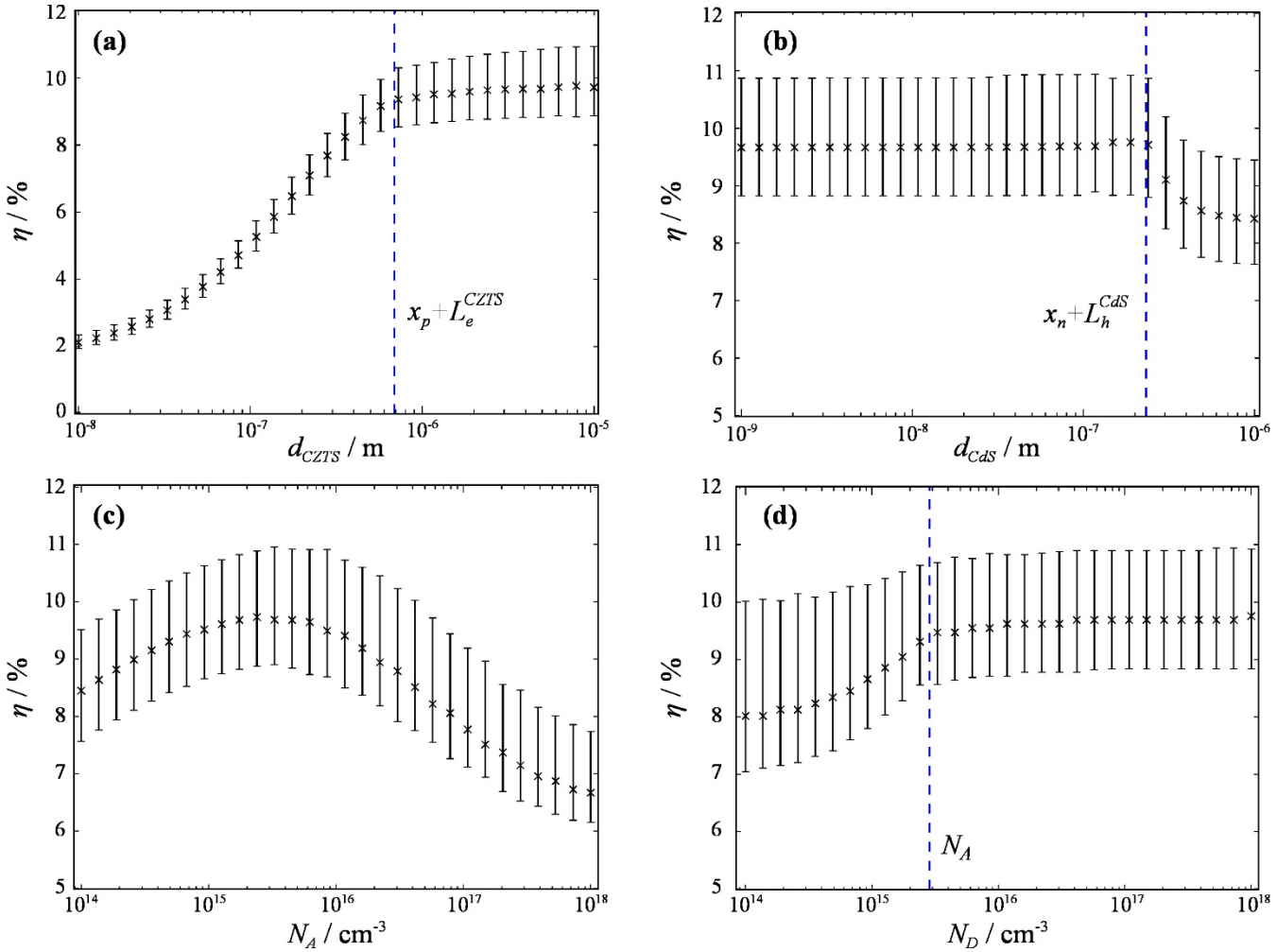

Figure 12: η in the proximity of η_{max}. (a) d_{CZTS}, (b) d_{CdS}, (c) N_A, and (d) N_D are independently varied, while the other three parameters are fixed to the values that achieve η_{max}. The blue vertical lines show where (a) $d_{CZTS} = x_{CZTS} + L_e^{CZTS}$, (b) $d_{CdS} = x_{CdS} + L_h^{CdS}$, and (d) $N_D = N_A$. The errors bars show the error due to the uncertainty of the input parameters and have different magnitudes above and below the mean values due to the non-linear dependence of η on the inputs.